# A graph-based formulation for computational characterization of bulk heterojunction morphology

Olga Wodo [a], Srikanta Tirthapura [b], Sumit Chaudhary [b,c], Baskar Ganapathysubramanian [a,b,*]

[a] Department of Mechanical Engineering, Iowa State University, Ames, IA, United States
[b] Department of Electrical and Computer Engineering, Iowa State University, Ames, IA, United States
[c] Department of Materials Science and Engineering, Iowa State University, Ames, IA, United States

## ARTICLE INFO

## ABSTRACT

To improve the efficiency of organic solar cells, it is essential to understand the role of morphology and to tailor fabrication process to get desired morphologies. In this context, a comprehensive set of computational tools to quantify and classify the 2D/3D heterogeneous internal structure of thin films is invaluable. We present a graph-based framework to efficiently compute a broad suite of physically meaningful morphology descriptors. These morphology descriptors are further classified according to the physical subprocesses within OSCs – photon absorption, exciton diffusion, charge separation, and charge transport. This approach is motivated by the equivalence between a discretized 2D/3D morphology and a *labeled*, *weighted*, *undirected graph*. We utilize this approach to pose six key questions related to structure characterization. These questions are the basis for a comprehensive suite of morphology descriptors. To advocate the appropriateness of the formulated suite, we correlate these morphology descriptors with analysis using a excitonic-drift–diffusion-based device model. A very high correlation between the fast graph-based approach and computationally intensive full scale analysis illustrates the potential of our formulation to rapidly characterize a large set of morphologies. Finally, our approach is showcased by characterizing the effect of thermal annealing on time-evolution of a model thin film morphology.

© 2012 Elsevier B.V. All rights reserved.

## 1. Introduction

Organic solar cells (OSC) fabricated from polymer–fullerene blends [1,2] represent a promising low-cost, rapidly deployable strategy for harnessing solar energy [3]. Along with synthesis of new organic semiconductors[1] and development of new device architectures[2], improvements in efficiencies have come from optimizing material processing to improve morphology. Improving morphology is crucial because all physical processes within an OSC (and thus the device performance) are a strong function of thin film morphology.

Most OSCs have bulk-heterojunction architecture (BHJ) [3,8,9]. BHJ consists of an electron donating polymer and electron accepting fullerene-derivatives usually intermixed with domains of the order of exciton diffusion length. The final morphology of electron-donor and electron-acceptor regions in the device strongly affects the power conversion efficiency of OSCs. This has its origin in the operating principle of organic solar cells (see Fig. 1), which can be broadly classified into three stages: (1) light absorption and exciton generation, (2) exciton diffusion to the donor–acceptor interface and dissociation into free charges, and (3) charge transport towards the electrodes.

---

* Corresponding author at: Department of Mechanical Engineering, Iowa State University, Ames, IA, United States. Tel.: +1 515 294 7442; fax: +1 515 294 3261.
   E-mail address: baskarg@iastate.edu (B. Ganapathysubramanian).
   URL: http://www3.me.iastate.edu/bglab/ (B. Ganapathysubramanian).
   [1] e.g., PBDTTT [4], PTB systems [5].
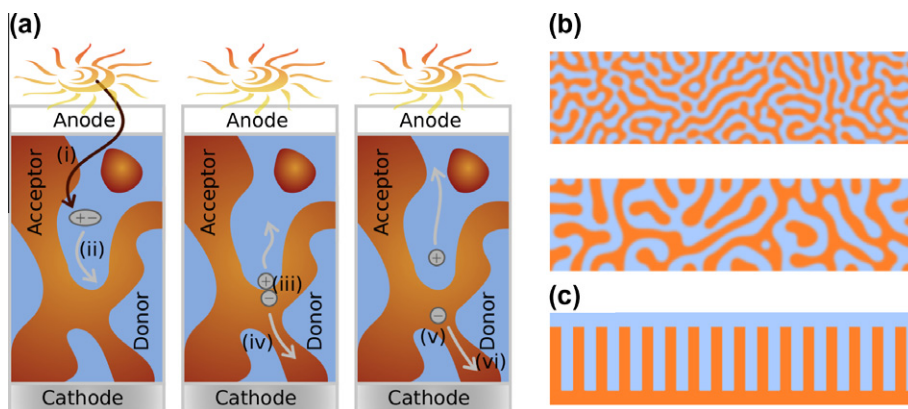   [2] e.g., inverted architecture [6], tandem cells [7].

**Fig. 1.** Link between bulk heterojunction morphology and photocurrent generation. Figure on left (a) lists the physical processes affected by the morphology: (i) exciton generation, (ii) exciton diffusion, (iii) exciton dissociation, (iv) charges separation, (v) charge transport, (vi) extraction of charges. Figure on right (b) shows two similar looking morphologies with very different features – number of isolated islands and regions connected to electrodes, tortuosity – which will lead to different device characteristics. (c) The cartoon of hypothesized ideal structure: perfectly-ordered tooth-structure. (For interpretation of the references to colour in this figure legend, the reader is referred to the web version of this article.)

Light absorption by photoactive material leads to creation of excitons. These excitons have a finite lifetime (before recombining due to Coulomb attraction) during which they can diffuse. Excitons dissociate to form useful free charges *only at the donor–acceptor interface* [10]. Thus, only those excitons that are created a short distance from the interface are able to reach the donor–acceptor interface and dissociate into free charge carriers. The final step of photocurrent generation is transport of free charge carriers to respective electrodes. Electrons travel only through electron-acceptor rich regions to the cathode, while holes travel only through electron-donor rich regions to the anode. Consequently, if charges are created in islands or "cul-de-sacs" with no direct connection to the appropriate electrode, they eventually recombine. Therefore, short and continuous pathways of electron-donor and electron-acceptor regions directly connected to appropriate electrodes are necessary for charge transport and extraction. Thus, every stage of the photovoltaic process is extensively affected by the morphology of the thin film.

Developing a comprehensive set of morphology descriptors provides means to better characterize, understand and quantify the role that morphology plays [11]. Progress in experimental characterization [12–14] and computational modeling [15–17] now allow *in situ* and *in silico* 3D reconstruction and imaging of the thin film morphology with unprecedented accuracy and resolution. A computational framework capable of constructing morphology descriptors, efficiently for large data sets, can enable deciphering the role of morphology on device performance. By extensive characterization of morphology we provide the ability to reduce the complex morphology into set of physically meaningful morphology descriptors, thus enabling easier comparison between morphologies. The ultimate goal is to provide a tool for rational tailoring of fabrication process, which is currently a major challenge. A complementary challenge is the search for an "optimal" morphology. In this context, exciting recent work [18] suggests that morphologies having equivalent descriptors (particularly, feature size) may have similar performance characteristics (seemingly turning the search for an optimal structure into that of optimal descriptors). This further emphasizes the necessity of rapid, efficient and comprehensive morphology characterization to enable linking structure and performance.

Detailed nanomorphology characterization is almost absent in the context of OSCs. There have only been a few attempts to characterize selected morphological properties affecting the final efficiency using (i) the autocorrelation function [19,14]; (ii) the interfacial area between electron-donor material and electron-acceptor material [20,21], and (iii) the fraction of volume connected to the relevant electrode [22]. While these quantities give important insight into the effect of morphology on device physics, they essentially provide only coarse information. For instance, the averaged feature size of morphology can be extracted from the autocorrelation function. The feature size allows to assess the propensity of excitons to reach the interface.[3] However, the averaged domain size does not distinguish between electron-donor and electron-acceptor regions. Similarly, the fraction of volume connected to relevant electrodes provides important insight into the charge transport by quantifying the useful regions of domain. However, this descriptor does not provide any quantitative information on the length or tortuosity of paths in the morphology. Quantifying the tortuosity of the morphology (of both electron-donor and electron-acceptor regions) is of particular interest, due to the finite life time of charges and the differences in the charge mobilities of electrons and holes.

In this paper, we provide a comprehensive suite of physically meaningful morphology descriptors, which reflect the complex nature of the BHJ and the underlying device physics. We formulate and implement a graph-based

---

[3] In practice the feature size is linked with the "exciton-diffusion length" which is around 10 nm for P3HT [23] (the best studied conjugated polymer in the context of OSCs). When the averaged feature size is comparable or smaller than exciton diffusion length, there is a high probability for high exciton dissociation. Otherwise, only a small fraction of excitons can physically reach the interface and contribute to current generation.

framework to efficiently construct this comprehensive suite. This approach is motivated by the equivalence between a discretized 2D/3D morphology image and a *labeled, weighted, undirected graph*. These morphology descriptors are further classified according to the physical subprocesses of the photovoltaic process: exciton diffusion, exciton dissociation into free charge carriers, and charge transport. We utilize this approach to pose six device-performance relevant questions to exhaustively characterize the morphology. The approach is showcased by characterizing the effect of thermal annealing on time-evolution of a thin film morphology.

## 2. A taxonomy of physically meaningful descriptors to characterize morphology

We broadly define four groups of morphology descriptors to characterize the nanomorphology: descriptors quantifying light absorption, exciton diffusion, exciton dissociation and charge transport:

- *Light absorption:* In most BHJs, light is absorbed by the electron-donor material to create excitons.[4] Thus, a natural descriptor is the fraction of electron-donor material within the active layer of the device.
- *Exciton diffusion:* A key metric that affects exciton diffusion is simply the distance to the nearest donor–acceptor interface.
- *Exciton dissociation:* To increase the number of separated charges, the length of the interface should be maximized. Thus, the most natural morphology descriptor reflecting the nature of exciton dissociation is the interfacial area.
- *Charge transport:* An ideal morphology should have following characteristics for good charge transport:
  - (i) *A percolating network* of electron-donor and electron-acceptor materials. The morphology should not have any "islands" or "cul-de-sacs" to minimize recombination. In other words, all donor and acceptor domains should be connected to relevant electrodes.
  - (ii) *Short paths* to both electrodes: This is important to minimize the possibility of recombination and also accounts for mean free path of carriers.
  - (iii) *Balanced paths* to avoid charge accumulation, that is, the electron and hole path lengths should be similar.

The above characterizations of an ideal morphology motivates the following descriptors: the fraction of useful domains, the distance charges travel from interface to electrodes via electron-donor or electron-acceptor regions, and the fraction of interface with complementary paths to both electrodes.

Such a categorization provides a clear physics-based rationale and provides succinct guidance for establishing

links between morphology and each constitutive subprocess in the photovoltaic process within an OSC. In the sequel, we develop efficient graph-based techniques to construct a suite of descriptors listed above. We formulate six questions related to the aforementioned subprocesses. These questions provide insight into the factors affecting the performance of the device:

- Q1 What is the fraction of light absorbing material? (affects absorption)
- Q2 What is the fraction of electron-donor material whose distance to the donor–acceptor interface is within a given range? (affects exciton diffusion)
- Q3 What is the interfacial area between donor and acceptor regions? (affects exciton dissociation)
- Q4a What is the fraction of donor domain connected to anode? (affects hole transport and extraction)
- Q4b What is the fraction of acceptor domain connected to cathode? (affects electron transport and extraction)
- Q5a What is the distance from donor–acceptor interface to the anode via donor domain only? (affects hole transport and extraction)
- Q5b What is the distance from donor–acceptor interface to the cathode via acceptor domain only? (affects electron transport and extraction)
- Q6 What is the fraction of interface which has complementary paths to both electrodes? (affects charge transport and extraction)

In the Supplementary information, we provide a detailed description of the methodology along with examples illustrating the characterization on several representative morphologies.

## 3. Linking morphology descriptors and performance

This constructed suite of morphology descriptors can further be used to construct performance indicators of a given morphology with respect to each subprocesses of the photovoltaic process. We detail each such indicator below.

### 3.1. Exciton diffusion and dissociation performance indicators

The first estimate is based on the maximum possible distance, $L_d$, an exciton can diffuse before it returns to ground state. In practice, $L_d$ is associated with the exciton diffusion length [23]. By finding the fraction of donor material within this distance to the donor–acceptor interface, we identify the fraction of donor material that can theoretically contribute to this stage. Donor material distributed beyond this distance to the interface has a significantly lower chance of being useful. Therefore, this quantity serves as a good upper bound on the exciton diffusion performance, $f_{diss}^{upp}$.

A more aggressive indicator, $f_{diss}^{est}$, can be computed by selecting a smaller distance, $L_m$, within which the exciton has a *high probability of reaching* the interface.[5] Both

---

[4] Electron acceptors also absorb light to create excitons. However, in most cases light absorption and exciton harvesting are very weak compared to donor material. This is the case for $PC_{61}BM$ – the most common acceptor [24].

[5] If $L_m$ is relatively small, i.e., 1 nm, then this bound can be associated with the interfacial area.

estimates are determined from Q2 defined in Section 2 (what is the fraction of domain with distance to interface shorter then given distance $d$?).

### 3.2. Charge transport performance indicator

Questions Q4 and Q6 from the previous section can be used to construct indicators of charge transport. An upper performance indicator for charge transport can be defined as *the fraction of useful regions* for charge transport, $f_{out}^{upp}$. Only regions which have a connection to the relevant electrode constitute paths for charges to travel and consequently can contribute to current generation. Thus, computing the fraction of domain satisfying this constraint defines an upper bound, $f_{out}^{upp}$.

This bound can be tightened by considering the complementary nature of the pathways, that is, by computing the fraction of donor–acceptor interface with continuous pathways to *both electrodes* (Q6), $f_{out}^{path}$. This is because if one type of charge-carrier is not transported to the electrode (due to islands, or "cul-de-sacs"), it affects the local electric potential and leads to non-uniform electric field in the device. This, in turn, influences the transport of the other type of charge carrier and increases charge recombination.

### 3.3. Absorption performance indicator

In an OSC, light is typically absorbed (to create useful excitons) only by one type of material-mostly by the electron donating polymer. Therefore, finding the fraction of donor material provides information on light absorption – $f_{abs}^{upp}$. Intensity of light decays exponentially as light traverses through the active-layer (see Supplementary information). We take this into account by introducing weight function, $a$, that assigns value, $a(v) = exp\left(-\frac{h(v)}{H_d}\right)$, to each vertex of $V$, where $h$ is the physical distance of a vertex, $v$, from the top surface, and $H_d$ is absorption coefficient that is a property of a given material. In this way, instead of counting all vertices (Q1), we count all vertices weighted by their attribute, $a(v)$. Calculated weighted fraction of donor material serves as more realistic absorption performance indicator, $f_{abs}^{est}$. We note that these are simple estimates which do not take into account the various possible designs for light trapping [25] and reflections. However, we argue that these metrics provide insights into the amount of light that can be absorbed by a given morphology.

The morphology descriptors and corresponding performance indicators detailed in this section allow for quick, hierarchical and comprehensive comparison between morphologies. Furthermore, these performance indicators can be used to filter massive data-sets of morphologies, and identify morphologies with the highest potential for efficient devices. Such a rapid prototyping stage for linking structure with properties can significantly enhance our understanding of OPV performance physics and help towards achieving high efficiency devices.

## 4. Analysis of BHJ morphology

In this section, we analyze a large set of morphologies that are representative of OSCs. For each morphology, we compute morphology indicators using the graph-based method detailed earlier. We then correlate these indicators with performance. We estimate performance by virtually interrogating each morphology under 1-sun condition. This is accomplished by solving a excitonic-drift–diffusion-based device model [26]. This correlation study allows us to pick three morphology indicators that (taken together) correlate well with the results of the performance analysis. We utilize these indicators to showcase how morphology characterization can then be used to rapidly link fabrication process with performance indicators on a model system.

### 4.1. Estimation of the morphology descriptors and correlating with performance

A key motivation to construct morphology descriptors is to facilitate quick characterization of morphology. In particular, we want to find physically meaningful morphology descriptors that can be used to filter/classify large morphology data sets. This allows selecting morphologies that show the highest potential for their specific application.

We start with a large set of 100 representative bulk heterojunction morphologies. These morphologies have vastly different features size, connectivity, and consequently photovoltaic properties. Six example morphologies are shown in Fig. 2. For each morphology we estimate performance under 1-sun condition using a excitonic-drift–diffusion model. We also compute performance indicators using the graph-based approach.
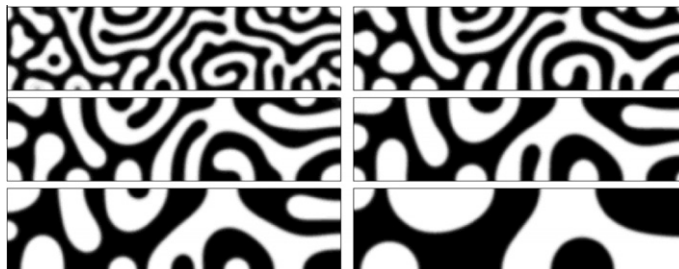


**Fig. 2.** Examples of six representative BHJ morphologies used in the analysis.

In case of graph-based approach, we focus on three morphology descriptors that quantify each stage of the photovoltaic process: weighted fraction of light absorbing material: $f_{w-abs}$, fraction of photoactive material within 10 nm distance to the interface: $f_{diss}$, and fraction of useful domains: $f_{out}$. We further define a "performance indicator" as product of these three fractions:

$$f = f_{w-abs} f_{diss} f_{out} \qquad (1)$$

Full scale analysis consists of computing the current–voltage characteristics of a morphology using the excitonic-drift–diffusion model [26–28]. We select the magnitude of short circuit current density, $|J_{sc}|$, as a quantity of interest for the comparison. The choice is motivated by two reasons. First, $J_{sc}$ is a direct measure of the device performance. In addition, the magnitude of short circuit current density is a quantity which is strongly affected by the morphology [20,29].

We compare the two approaches by testing how correlated the performance indicator $f$ is to $J_{sc}$. In Fig. 3, we plot the correlation between $J_{sc}$ and $f$ for all hundred morphologies. Morphologies with low efficiencies have low $|J_{sc}|$. Similarly, morphologies with high efficiencies also show high $|J_{sc}|$. The correlation coefficient between $|J_{sc}|$ and $f$ is very high (95.57%). *This implies that $f$ is a good marker for $J_{sc}$. What is noteworthy is that for each morphology, the calculations of $f$ takes around 2 s, while full scale analysis takes around 8 h.*

One should, however, note that the graph-based approach does not take into account several physical aspects of the photovoltaic process, such as recombination or effect of electric field. Nevertheless, this approach performs very well to rank order morphologies. We illustrate this ability to rank order morphologies by further analyzing two example morphologies that have good and bad properties. We mark them as G and B, respectively, in Fig. 3. These two morphologies are shown in Fig. 4. In the same figure, we also include the full current–voltage curve for these two morphologies (computed using full scale analysis), as well as detailed characterization (using graph-based method).

Both morphologies have similar characteristics of light absorption. The main difference between them comes from the fraction of the donor material which is close to the donor–acceptor interface. In case of good morphology (G), almost all donor-material can contribute to exciton dissociation and subsequently charge generation. On the other hand, only 35.9% of donor material can contribute to exciton dissociation in the bad morphology (B). This is because the morphology is characterized by large bulky domains. The morphology marked B also has significantly shorter interface length (Q3): 906 nm (comparing to 4202 nm for morphology marked G). All these indicate very poor exciton dissociation capabilities, which is seen as a low $f_{diss}$. On the other hand, bulky domains result in shorter, direct paths for charge transport. Notice that the B-morphology shows consistently higher values for all charge transport morphology descriptors: Q4, Q5, Q6 (table in Fig. 4). Interestingly, this low $f_{diss}$ of B-morphology cannot be compensated by better charge transport properties ($f_{out} = 79\%$) of the bad morphology.
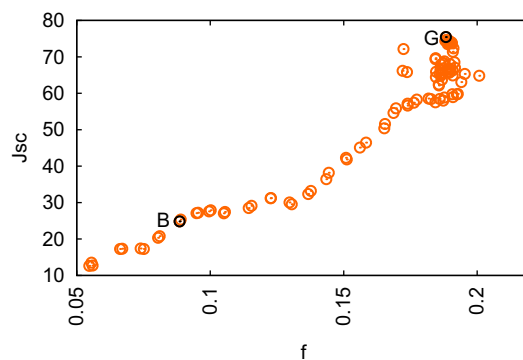


**Fig. 3.** Correlation between performance indicators estimated using our approach and short circuit current calculated using full scale analysis – excitonic-drift–diffusion model. Characteristics for two selected morphologies for detailed analysis are marked G (good morphology) and B (bad morphology).

One should additionally note that detailed morphology characterization reveals the potential reasons for good or bad performance. By analyzing set of morphology we acquire a hierarchical characterization of the morphology with relation to each stage of photovoltaic phenomena. In contrast, full scale excitonic-drift–diffusion analysis provides the final performance estimation, such as short circuit current (one value versus a set of morphology descriptors).

### 4.2. Linking thermal annealing with structure

In this section, we showcase how the performance indicators can be used to identify the optimal conditions of the fabrication process. Specifically, we are interested in a rapid investigation of multiple morphologies and selecting the best morphology and its associated fabrication conditions.

We start with two large sets of morphologies with blend ratios of 1:1 and 1:0.82 (acceptor:donor), respectively (Fig. 5). Each set of morphologies depicts time evolution during the process of thermal annealing of this model system. Thermal annealing is one of the important postfabrication processes utilized in OSCs to improve power conversion efficiencies [30–32].

We choose these two blend ratios because they represent two types of morphologies – percolated morphology and morphology with islands. Intuitively, the former is more suitable for OSC than the latter, for all times during annealing. This is because the latter structure has more islands not connected to relevant electrodes and cannot provide useful pathways for charges. Each set consists of nine hundred images. Each image represents a morphology of size 100 nm × 1000 nm. Fig. 5 depicts six representative morphologies for each type.

We estimate all morphology descriptors (for all 1800 morphologies) and plot them in Fig. 5 ordering them accordingly to blend ratio and corresponding annealing time.

In Fig. 5(b), we estimate the *exciton dissociation* performance indicator. Thermal annealing increases the feature

Cumulative histogram of distances from any point in donor region to the interface

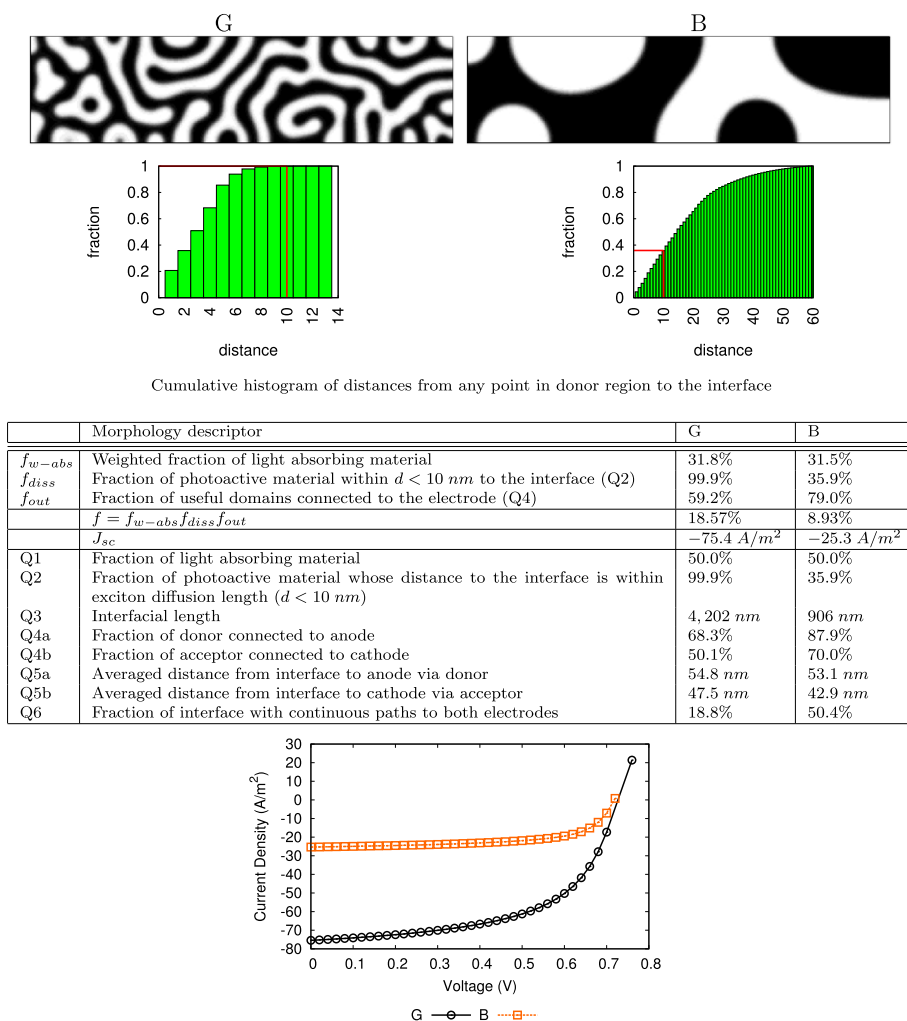| | Morphology descriptor | G | B |
|---|---|---|---|
| $f_{w-abs}$ | Weighted fraction of light absorbing material | 31.8% | 31.5% |
| $f_{diss}$ | Fraction of photoactive material within $d < 10\ nm$ to the interface (Q2) | 99.9% | 35.9% |
| $f_{out}$ | Fraction of useful domains connected to the electrode (Q4) | 59.2% | 79.0% |
| | $f = f_{w-abs} f_{diss} f_{out}$ | 18.57% | 8.93% |
| | $J_{sc}$ | $-75.4\ A/m^2$ | $-25.3\ A/m^2$ |
| Q1 | Fraction of light absorbing material | 50.0% | 50.0% |
| Q2 | Fraction of photoactive material whose distance to the interface is within exciton diffusion length ($d < 10\ nm$) | 99.9% | 35.9% |
| Q3 | Interfacial length | $4,202\ nm$ | $906\ nm$ |
| Q4a | Fraction of donor connected to anode | 68.3% | 87.9% |
| Q4b | Fraction of acceptor connected to cathode | 50.1% | 70.0% |
| Q5a | Averaged distance from interface to anode via donor | $54.8\ nm$ | $53.1\ nm$ |
| Q5b | Averaged distance from interface to cathode via acceptor | $47.5\ nm$ | $42.9\ nm$ |
| Q6 | Fraction of interface with continuous paths to both electrodes | 18.8% | 50.4% |



**Fig. 4.** Example to two morphologies with high (left) and low (right) potential for organic solar cells with detailed characterization.

size. Increasing feature size does not affect exciton dissociation as long as the feature size is smaller than the exciton diffusion length. Beyond this point, less domain is located within this distance to the donor–acceptor interface, thus decreasing exciton dissociation. We observe this trend for both data sets as seen in Fig. 5(b) in which $f_{diss}^{upp}$ and $f_{diss}^{est}$ are plotted. It is interesting to note that even though the type of morphology is significantly different in both cases, the estimates are comparable.

Finally, we compare the two data sets with respect to *charge transport indicators*. In Fig. 5(c), we compare two data sets with respect to fraction of useful regions ($f_{out}^{upp}$) and fraction of the donor–acceptor interface with complementary paths ($f_{out}^{path}$). We notice that the coarsening of morphology improves the quality of paths as well as the total fraction of useful domains, as expected. However, unlike estimates of light absorption and exciton dissociation ($f_{abs}$ and $f_{diss}$), charge transport is clearly affected by the type of morphology. For blend ratio 1:0.82, $f_{out}^{upp}$ is unable to reach 100%. In contrast, for percolated structure (blend ratio 1:1), it is possible for the entire active layer to be

useful and connected to appropriate electrodes. Both estimates $f_{out}^{upp}$ and $f_{out}^{path}$ are able to discern between classes of morphology.

Additionally, we notice that for blend ratio 1:0.82 the fraction of useful domain cannot be improved significantly in the course of thermal annealing. In contrast, such improvement is possible for interpenetrated structure (1:1). This is very interesting and shows that not every system can be improved by thermal annealing. This is particularly important in the context of tailoring the fabrication process.

To summarize the analysis, we cumulate all factors and compare the "total performance indicator". In Fig. 5(d), we present two plots of the total estimates: $f^{upp}$ and $f^{est}$. Estimate $f^{upp}$ is constructed using only the upper bounds of performance indicators: $f_{abs}^{upp}$, $f_{diss}^{upp}$, $f_{out}^{upp}$, while $f^{est}$ uses the following constitutive estimates: $f_{abs}^{est}$, $f_{diss}^{est}$, $f_{out}^{path}$. For both blend ratios, performance indicator increases initially, reaches a maximum and subsequently decreases. This trend is due to two competing properties: exciton dissociation and charge transport. The initial increase is because
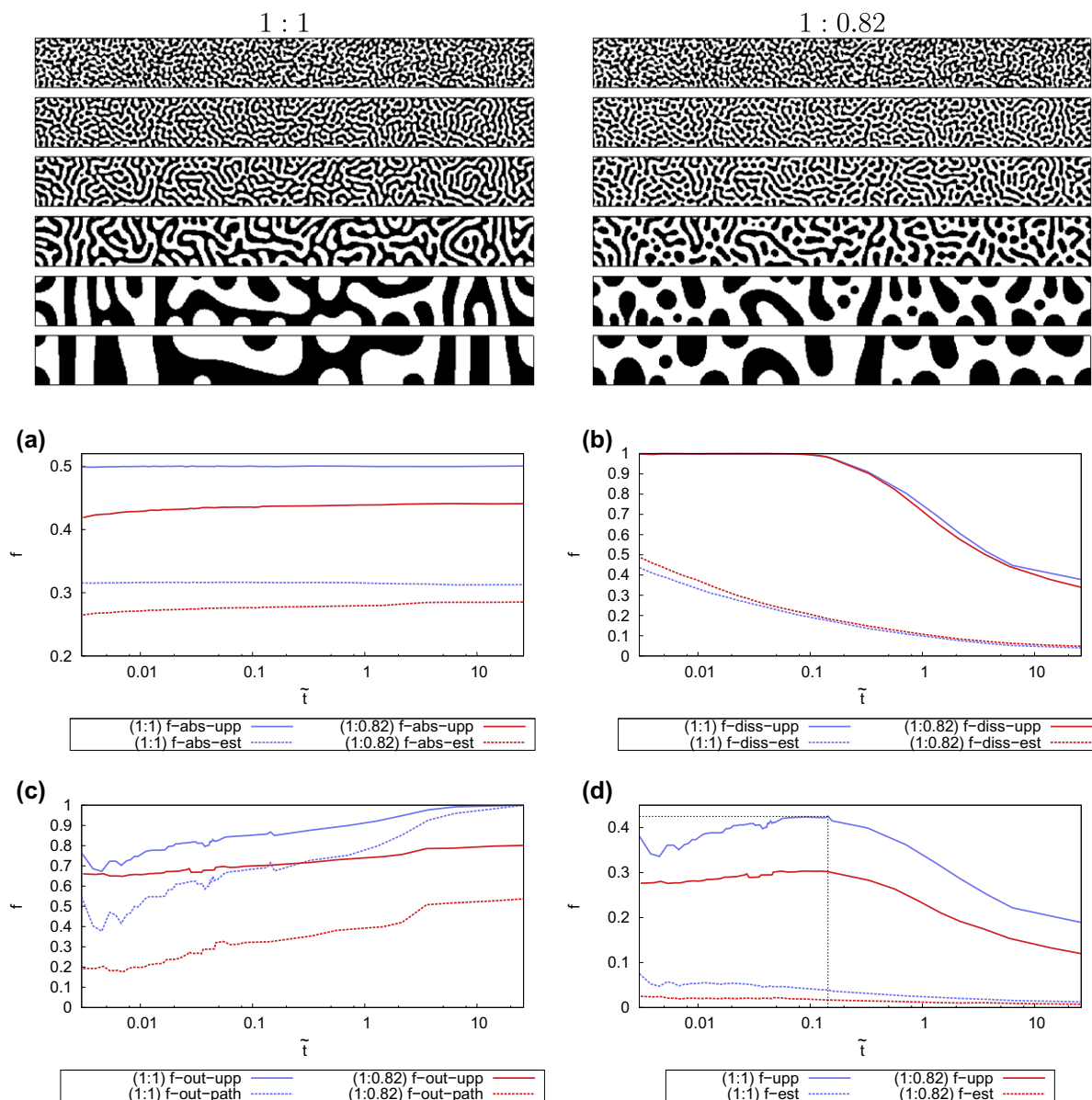
$1 : 1$　　　　　　　　　　　　　　　　　$1 : 0.82$





**Fig. 5.** Representative two-phase morphology evolution obtained via numerical simulation of thermal annealing for two blend ratios (1:1 and 1:0.82) from early stages (first row) untill the final time (consecutive rows). Efficiencies as a function of annealing time $\bar{t}$ (dimensionless) for two different blend ratios. Plots show estimates of efficiencies for blend ratios 1:1 (blue) and 1:0.82 (red). (a) Light absorption, (b) exciton dissociation, (c) charge transport, and (d) total performance indicator with maximum value marked. (For interpretation of the references to colour in this figure legend, the reader is referred to the web version of this article.)

of improved pathways which result in increased charge transport properties. During this period, exciton dissociation remains unaltered and high. As morphology evolution proceeds further, exciton dissociation deteriorates rapidly (due to increased feature size). The rate at which exciton dissociation deteriorates is much faster than improvement of charge transport. Consequently, the total performance indicator also deteriorates. This shows that during thermal annealing, charge transport is the initial bottleneck, agreeing with a recent work by Chen et al. [30]. Beyond a certain point during annealing, exciton dissociation becomes the

bottleneck and cannot be compensated by the improving charge transport.

It is also evident that the indicators are significantly lower for particle-like structures than interpenetrated structures. This confirms the importance of morphology control to ensure an interpenetrated structure with minimal number of isolated regions.

From Fig. 5, the optimal morphology occurs at $\bar{t} = 0.144$ with constitutive performance indicators of: $f_{abs}^{upp} = 50\%$, $f_{diss}^{upp} = 98\%$ and $f_{out}^{upp} = 86\%$. It is interesting to notice that the product of $f_{diss}^{upp}$ and $f_{out}^{upp}$ translates to a (rough) estimate

of the internal quantum efficiency of 84% which is in good agreement with the internal quantum efficiency reported for the best devices obtained using thermal annealing [3,33,34].

## 5. Limitations, extensions and perspectives

The methodology detailed in this paper proposes a simple, graph-based approach to morphology characterization. A graph-based approach offers the ability to rapidly convert a complex morphology into a set of physically meaningful morphology descriptors reflecting the multi-stage photovoltaic process in organic blends. Nevertheless, it has to be recognized that this framework is a simple mechanistic approach that is built on physics-based intuition. This carries with it an associated set of limitations that need to be appreciated. In particular, the current framework does not take into account crystallinity and anisotropy, nor does it account for the effect of electric field, and the various methods of recombination (geminate, non-geminate). Additionally, we assume in the analysis that the morphology consists of two phases: electron donor-rich and electron-accepting rich phases, and analyze a binary morphology.[6]

While cognizant of these limitations, we emphasize that this framework can be extended to address most of these limitations. We briefly sketch how this can be accomplished, while postponing a detailed analysis for a subsequent publication. A graph-based approach can be naturally extended by adding additional properties to vertices and edges and by expanding the set of labels (see Supplementary information for details on graph definition). For example, by extending the set of vertex labels (from simple black/white to a grayscale), multi-phase morphology can be easily represented as a graph. Moreover, crystallinity effects can be investigated by defining an additional property (degree of crystallinity) with each vertex. Similarly, anisotropy effects can be included by defining direction-dependent edge properties. Analogously, knowledge of the molecular organization, e.g. distribution and topology of main backbones of polymer, can be reflected in weighted edges that will result in a more accurate (charge transport) path characterization. Furthermore, a graph-based approach offers not only the capability to include more complex representation of morphology but also the flexibility to design additional morphology descriptors that reflect complex physics in more detail. In particular, we can extend the descriptors to account for geminate and non-geminate recombination. In this work, we have detailed the methodology to determine the fraction of donor phase within a distance of exciton diffusion length. This quantity naturally serves as a coarse indicator of geminate recombination. Noting that the probability of an exciton reaching the donor–acceptor interface depends on the distance that an exciton has to travel, and that excitons travel via a diffusion process – a descriptor of geminate recombination can be constructed by weighting the fraction of donor phase which is a given distance, $d$, away from the interface. This weight represents the probability of an exciton traveling a distance $d$ (this probability will be a Gaussian distribution since excitons travel by a diffusion process). Similarly, noting that non-geminate recombination (where dissociated charges traveling to respective electrodes recombine) depends on the charge transport path length and potential obstacles along the path – a natural descriptor to quantify non-geminate recombination is the tortuosity of the path distribution.

We envision this framework to complement (and not replace) full-scale analysis of the device physics (using experimental techniques or sophisticated computational models). By reducing the complex morphology into a set of descriptors (histograms and scalars), this framework enables multi-criteria morphology ordering and comparison. Correlating selected morphological features with experimental performance characteristics will enable a better understanding of the role of morphology on device performance. This could result in the ability to systematically establish link between fabrication, structure and performance. We also envision the application of such a graph-based morphology characterization framework in other areas involving transport in heterogeneous structures, such as percolation pathways in geomechanics, porous media, and drug release from polymeric membranes.

## 6. Conclusion

A comprehensive set of computational tools to rapidly quantify and classify the 2D/3D heterogeneous internal structure of OSC thin films is invaluable in linking process, structure and property. Development of such a framework is challenging because of the coupled and contradictory effect of morphology on light absorption, exciton dissociation and charge transport. In this paper we addressed these challenges and provided a highly efficient framework based on graph theory to computationally characterize the morphology. In particular:

1. We presented the first such broad analysis of the BHJ morphological features, where all subprocesses are quantified and analyzed individually.
2. We categorized physically meaningful morphology into four main groups.
3. We formulated six questions to provide a comprehensive characterization of BHJ using a graph approach.
4. We additionally employed the questions to construct performance indicators of all constitutive subprocesses of the photovoltaic effect in organic materials.
5. We compare estimates with full scale excitonic-drift–diffusion-based analysis, to verify this approach. A very high correlation between the fast graph-based estimates and computation intensive full scale analysis illustrate the potential of our formulation to rapidly classify a large set of morphologies.
6. We identified the bottlenecks in the morphology evolution during thermal annealing, which is one the major fabrication processes, through the individual analysis of subprocesses.

---

[6] While such an assumption is in line with the currently accepted portrait of a ideal device as consisting of pure donor and acceptor phases with well-defined interfaces, recent work (particularly for the P3HT:PCBM system) suggests the existence of the amorphous third phase [35–38].

## Acknowledgments

## Appendix A. Supplementary data

Supplementary data associated with this article can be found, in the online version, at http://dx.doi.org/10.1016/j.orgel.2012.03.007.

## References

[1] G. Dennler, M. Scharber, C. Brabec, Polymer–fullerene bulk-heterojunction solar cells, Advanced Materials 21 (2009) 1–16.
[2] H. Hoppe, N. Sariciftci, Organic solar cells: an overview, Journal of Materials Research 19 (2004) 1924–1945.
[3] S. Park, A. Roy, S. Beaupre, S. Cho, N. Coates, J. Moon, D. Moses, M. Leclerc, K. Lee, A. Heeger, Bulk heterojunction solar cells with internal quantum efficiency approaching 100%, Nature Photonics 3 (2009) 297–302.
[4] H.-Y. Chen, J. Hou, S. Zhang, G. Liang, Y. Yang, Y. Yang, L. Yu, Y. Wu, G. Li, Polymer solar cells with enhanced open-circuit voltage and efficiency, Nature Photonics 3 (2009) 649–653.
[5] Y. Liang, D. Feng, Y. Wu, S.-T. Tsai, G. Li, C. Ray, L. Yu, Highly efficient solar cell polymers developed via fine-tuning of structural and electronic properties, Journal of the American Chemical Society 131 (2009) 7792–7799.
[6] S. Hau, H.-L. Yip, J. Zou, A.-Y. Jen, Indium tin oxide-free semi-transparent inverted polymer solar cells using conducting polymer as both bottom and top electrodes, Organic Electronics 10 (2009) 1401–1407.
[7] D. Cheyns, B.P. Rand, P. Heremans, Organic tandem solar cells with complementary absorbing layers and a high open-circuit voltage, Applied Physics Letters 97 (2010) 033301.
[8] G. Li, V. Shrotriya, J. Huang, Y. Yao, T. Moriarty, K. Emery, Y. Yang, High-efficiency solution processable polymer photovoltaic cells by self-organization of polymer blends, Nature Materials 4 (2005) 864–868.
[9] J. Peet, J. Kim, N. Coates, W. Ma, D. Moses, A. Heeger, G.C. Bazan, Efficiency enhancement in low-bandgap polymer solar cells by processing with alkane dithiols, Nature Materials 6 (2007) 497–500.
[10] D. Hertel, H. Bassler, Photoconduction in amorphous organic solids, ChemPhysChem 9 (2008) 666–688.
[11] S. Torquato, Random Heterogeneous Materials, Springer, 2002.
[12] B. Andersson, A. Herland, S. Masich, O. Inganas, Imaging of the 3D nanostructure of a polymer solar cell by electron tomography, Nano Letters 9 (2009) 853–855 (PMID: 1911991).
[13] S. von Bavel, E. Sourty, G. de With, J. Loos, Three-dimensional nanoscale organization of bulk heterojunction polymer solar cells, Nano Letters 9 (2009) 507–513.
[14] J. Moon, J. Lee, S. Cho, J. Byun, A. Heeger, "Columnlike" structure of the cross-sectional morphology of bulk heterojunction materials, Nano Letters 9 (2009) 230–234.
[15] M. Tsige, G.S. Grest, Solvent evaporation and interdiffusion in polymer films, Journal of Physics: Condensed Matter 17 (2005) S4119.
[16] S. Peumans, P. Uchida, S. Forrest, Efficient bulk heterojunction photovoltaic cells using small-molecular-weight organic thin films, Nature 425 (2003) 158–162.
[17] O. Wodo, B. Ganapathysubramanian, Modeling morphology evolution during solvent-based fabrication of organic solar cells, Computational Materials Science 55 (2012) 113–126.
[18] B. Ray, M.A. Alam, Random vs regularized OPV: limits of performance gain of organic bulk heterojunction solar cells by morphology engineering, Solar Energy Materials and Solar Cells 99 (2012) 204–212.
[19] W. Ma, C. Yang, A. Heeger, Spatial Fourier-transform analysis of the morphology of bulk heterojunction materials used in plastic solar cells, Advanced Materials 19 (2007) 1387–1390.
[20] B. Lei, Y. Yao, A. Kumar, Y. Yang, V. Ozolins, Quantifying the relation between the morphology and performance of polymer solar cells using Monte Carlo simulations, Journal of Applied Physics 104 (2008) 024504.
[21] L. Meng, Y. Shang, Q. Li, Y. Li, X. Zhan, Z. Shuai, R.G.E. Kimber, A.B. Walker, Dynamic Monte Carlo simulation for highly efficient polymer blend photovoltaics, The Journal of Physical Chemistry B 114 (2010) 36–41.
[22] S. von Bavel, E. Sourty, G. de With, K. Frolic, J. Loos, Relation between photoactive layer thickness, 3D morphology, and device performance in P3HT/PCBM bulk-heterojunction solar cells, Macromolecules 42 (2009) 7396–7403.
[23] P.E. Shaw, A. Ruseckas, I.D.W. Samuel, Exciton diffusion measurements in poly(3-hexylthiophene), Advanced Materials 20 (2008) 3516–3520.
[24] G.F. Burkhard, E.T. Hoke, S.R. Scully, M.D. McGehee, Incomplete exciton harvesting from fullerenes in bulk heterojunction solar cells, Nano Letters 9 (2009) 4037–4041.
[25] S.-B. Rim, S. Zhao, S.R. Scully, M.D. McGehee, P. Peumans, An effective light trapping configuration for thin-film solar cells, Applied Physics Letters 91 (2007) 243501.
[26] H.K. Kodali, B. Ganapathysubramanian, Computer simulation of heterogeneous polymer photovoltaic devices, Modelling and Simulation in Materials Science and Engineering 20 (2012) 035015.
[27] G.A. Buxton, N. Clarke, Computer simulation of polymer solar cells, Modelling and Simulation in Materials Science and Engineering 13 (2007).
[28] J. Williams, A.B. Walker, Two-dimensional simulations of bulk heterojunction solar cell characteristics, Nanotechnology 19 (2008) 424011.
[29] G. Buxton, N. Clarke, Predicting structure and property relations in polymeric photovoltaic devices, Physical Review B 74 (2006) 1–5.
[30] L. Chen, Z. Hong, G. Li, Y. Yang, Recent progress in polymer solar cells: manipulation of polymer:fullerene morphology and the formation of efficient inverted polymer solar cells, Advanced Materials 21 (2009) 1434–1449.
[31] A. Moule, K. Meerholz, Controlling morphology in polymer–fullerene mixtures, Advanced Materials 20 (2008) 240–245.
[32] W. Ma, C. Yang, X. Gong, K. Lee, A. Heeger, Thermally stable, efficient polymer solar cells with nanoscale control of the interpenetrating network morphology, Advanced Functional Materials 15 (2005) 1617–1622.
[33] Y. Liang, Z. Xu, J. Xia, S.-T. Tsai, Y. Wu, G. Li, C. Ray, L. Yu, For the bright future-bulk heterojunction polymer solar cells with power conversion efficiency of 7.4%, Advanced Materials 22 (2010) E135–E138.
[34] J. Hou, H.-Y. Chen, S. Zhang, R.I. Chen, Y. Yang, Y. Wu, G. Li, Synthesis of a low band gap polymer and its application in highly efficient polymer solar cells, Journal of the American Chemical Society 131 (2009) 15586–15587.
[35] W. Yin, M. Dadmun, A new model for the morphology of P3HT/PCBM organic photovoltaics from small-angle neutron scattering: rivers and streams, ACS Nano 5 (2011) 4756–4768.
[36] M. Pfannmoller, H. Flugge, G. Benner, I. Wacker, C. Sommer, M. Hanselmann, S. Schmale, H. Schmidt, F.A. Hamprecht, T. Rabe, W. Kowalsky, R.R. Schroder, Visualizing a homogeneous blend in bulk heterojunction polymer solar cells by analytical electron microscopy, Nano Letters 11 (2011) 3099–3107.
[37] B.A. Collins, Z. Li, C.R. McNeill, H. Ade, Fullerene-dependent miscibility in the silole-containing copolymer psbtbt-08, Macromolecules 44 (2011) 9747–9751.
[38] D. Chen, F. Liu, C. Wang, A. Nakahara, T.P. Russell, Bulk heterojunction photovoltaic active layers via bilayer interdiffusion, Nano Letters 11 (2011) 2071–2078.